INTERNATIONAL JOURNAL FOR NUMERICAL METHODS IN FLUIDS
Int. J. Numer. Meth. Fluids 2000; **32**: 691–709

Analysis of high speed non-equilibrium chemically reacting gas flows. Part II. A finite volume/finite element model and numerical studies

Christophe Harlé, Graham F. Carey* and Philip L. Varghese

CFD Laboratory, ASE/EM Department, WRW 301, The University of Texas at Austin, Austin, TX 78712, U.S.A.

SUMMARY

In this part, a new hybrid numerical model for solving the two-dimensional axisymmetric Navier–Stokes equations for a multi-species reacting gas out of thermal and chemical equilibrium is constructed. The formulation is based on a mixed finite volume/finite element formulation for unstructured meshes. The convective flux is treated with an approximate Osher–Riemann solver, and the other fluxes are treated using $P1$ finite elements. New aspects of the extension of the Osher–Riemann solver are presented here. This scheme was used for the benchmark model comparison in Part I, and is applied here to hypersonic (Mach 25) flow past a two-dimensional ellipse and a hemispherically blunted body at sea level. Copyright © 2000 John Wiley & Sons, Ltd.

KEY WORDS: gas flow; flux; hybrid numerical model; non-equilibrium

1. INTRODUCTION

Over the last decade, several methods have been proposed for solving two-dimensional reacting flows for combustion and hypervelocity problems [1–3] using finite difference formulations [4,5], finite volume schemes [6–9], or streamline upwind Petrov–Galerkin (SUPG) finite element methods [10]. Combustion flows are mostly subsonic or transonic, and assume thermal equilibrium. In the present work, focus is on the computation of high speed flows out of chemical and thermal equilibrium, for which the model system of partial differential equations (PDEs) is hyperbolic with a highly non-linear right-hand-side source term.

The method proposed in the present work is an extension of a hybrid finite volume/$P1$ finite element formulation introduced by Angrand and Dervieux [11,12] for perfect inviscid gases. The new formulation presented here includes three main aspects. Firstly, it extends the finite volume/finite element method to axisymmetric reacting flows. Secondly, the convective flux is

* Correspondence to: CFD Laboratory, ASE/EM Department, WRW 301, The University of Texas at Austin, Austin, TX 78712, U.S.A.

Received 11 August 1995
Revised 1 June 1998

treated with an upwind cell-centered scheme using a finite volume approach based on the scheme of Osher extended to non-equilibrium flows. In particular, the treatment of the intermediate states requires fewer assumptions than the work of Abgrall [13]. The other terms are treated using a finite element approximation. Thirdly, the convective and viscous fluxes are linearized within a time step to allow faster convergence.

2. PROBLEM FORMULATION

Part I described the equations governing a reacting gas out of thermal and chemical equilibrium. In this part, the case of a five-species gas is first considered, and then it is assumed that the vibrational energies of the molecular species are described by the same vibrational temperature. Therefore, only one vibrational energy equation is needed. For an axisymmetric problem, the vector momentum equation gives an axial and a radial equation. Thus, nine coupled PDEs are obtained, which may be written in vector form as

$$\frac{\partial \boldsymbol{W}}{\partial t} + \nabla \cdot (\boldsymbol{F}(\boldsymbol{W}) + \boldsymbol{V}(\boldsymbol{W})) = \Omega_c(\boldsymbol{W}) \tag{1}$$

where $\boldsymbol{W}$ is the vector of conservative variables, $\boldsymbol{F}$ and $\boldsymbol{V}$ are the convective and viscous fluxes respectively, and Ω_c is the source term due to chemical and thermal non-equilibrium. Hence, we write

$$\boldsymbol{W} = (\rho_i, \rho \boldsymbol{u}, E, E_{v1})^T \tag{2}$$

with $1 \leq i \leq ns$, where ns is the total number of chemical species of the gas, ρ_i is the density of species i, $\boldsymbol{u}$ is the mean average velocity, E is the total energy, and E_{v1} is the vibrational energy of the species whose vibrational energy is 'tracked'. Note that (1) does not distinguish formally between a two-dimensional and an axisymmetric two-dimensional problem. For computational convenience, the axisymmetric equation can be expressed in the form

$$\frac{\partial \boldsymbol{W}}{\partial t} + \tilde{\nabla} \cdot (\boldsymbol{F}(\boldsymbol{W}) + \boldsymbol{V}(\boldsymbol{W})) + \frac{1}{r} \boldsymbol{H}(\boldsymbol{W}) = \Omega_c(\boldsymbol{W}) \tag{3}$$

where $\tilde{\nabla} \cdot$ is the divergence operator for a two-dimensional problem, and r is the radial co-ordinate.

Setting

$$(\boldsymbol{F}(\boldsymbol{W}) + \boldsymbol{V}(\boldsymbol{W})) \cdot \tilde{\nabla} r - \boldsymbol{H}(\boldsymbol{W}) = \boldsymbol{S}(\boldsymbol{W}) \tag{4}$$

Equation (3) becomes

$$r \frac{\partial \boldsymbol{W}}{\partial t} + \tilde{\nabla} \cdot ((\boldsymbol{F}(\boldsymbol{W}) + \boldsymbol{V}(\boldsymbol{W}))r) = r\Omega_c(\boldsymbol{W}) + \boldsymbol{S}(\boldsymbol{W}) \tag{5}$$

In the following, the 'tilde' will be dropped and ∇ will be used to indicate the two-dimensional operator.

The solution is now sought in the two-dimensional $r-z$ section Ω of the three-dimensional domain D. For axisymmetric flows, the r and z components of $\boldsymbol{F}$ and $\boldsymbol{V}$ are

$$\boldsymbol{F}(\boldsymbol{W})=\begin{bmatrix} \rho_i u_r & \rho_i u_z \\ \rho u_r^2+p & \rho u_r u_z \\ \rho u_r u_z & \rho u_z^2+p \\ u_r(E+p) & u_z(E+p) \\ u_r E_{v1} & u_z E_{v1} \end{bmatrix}, \qquad \boldsymbol{V}(\boldsymbol{W})=-\begin{bmatrix} \rho_i w_{ir} & \rho_i w_{iz} \\ \tau_{rr} & \tau_{rz} \\ \tau_{zr} & \tau_{zz} \\ V_{Er} & V_{Ez} \\ V_{E_{v1}r} & V_{E_{v1}z} \end{bmatrix} \tag{6}$$

Here

$$V_{Er}=\tau_{rr}u_r+\tau_{rz}u_z+q_r+\sum_i \rho_i h_i w_{ir} \tag{7}$$

$$V_{Ez}=\tau_{zr}u_r+\tau_{zz}u_z+q_z+\sum_i \rho_i h_i w_{iz} \tag{8}$$

and

$$\boldsymbol{V}_{E_{v1}}=(V_{E_{v1}r},\, V_{E_{v1}z})^T=\boldsymbol{q}_v+E_{v1}\boldsymbol{w}_1 \tag{9}$$

The source term due to non-equilibrium effects is $\Omega(\boldsymbol{W})=(\Omega_{ci},\,0,\,0,\,0,\,\Omega_v)^T$ and the axisymmetric source term is $\boldsymbol{H}(\boldsymbol{W})=-(\rho_i w_{ir},\,H_r,\,H_z,\,H_E,\,H_{Ev})^T$ with

$$H_r=-\rho u_r^2+\tau_{rr}-\tau_{\theta\theta}-\frac{2}{3}\frac{\partial(\mu u_r)}{\partial r} \tag{10}$$

$$H_z=-\rho u_r u_z+\tau_{rz}-\frac{2}{3}\frac{\partial(\mu u_r)}{\partial z} \tag{11}$$

$$H_E=(E+p)u_r+u_r\tau_{rr}+u_z\tau_{rz}-q_r-\frac{2}{3}\mu\frac{u_r^2}{r}-r\frac{\partial}{\partial r}\left(\frac{2}{3}\mu\frac{u_r^2}{r}\right)-r\frac{\partial}{\partial z}\left(\frac{2}{3}\mu\frac{u_r u_z}{r}\right) \tag{12}$$

$$H_{Ev}=-E_{v1}u_r+q_{vr}+E_{v1}w_{1r} \tag{13}$$

and

$$\tau_{\theta\theta}=\frac{2}{3}\mu\left(-\nabla\cdot\boldsymbol{u}+2\frac{u_r}{r}\right) \tag{14}$$

The source term is $\boldsymbol{S}(\boldsymbol{W})=(0,\ldots,0,\,S_r,\,S_z,\,S_E,\,0)^T$ with

$$S_r = p - \tau_{\theta\theta} - \frac{2}{3}\frac{\partial(\mu u_r)}{\partial r} \tag{15}$$

$$S_z = -\frac{2}{3}\frac{\partial(\mu u_r)}{\partial z} \tag{16}$$

$$S_E = \frac{2}{3}\mu\frac{u_r^2}{r} + r\left(\frac{\partial}{\partial r}\left(\frac{2}{3}\mu\frac{u_r^2}{r}\right) + \frac{\partial}{\partial z}\left(\frac{2}{3}\mu\frac{u_r u_z}{r}\right)\right) \tag{17}$$

In Equations (6)–(17), the physical and chemical models defined in Part I apply.

A weak integral formulation of (5) can be constructed on a discretization of elements in the usual way. We then have the following discrete form for the axisymmetric problem:

Find $\boldsymbol{w}_h \in G_h(\Omega)$, such that

$$\int_\Omega \frac{\partial \boldsymbol{w}_h}{\partial t}\varphi_i r \, \mathrm{d}\Omega + \int_{C_i} \nabla\cdot(r\boldsymbol{F}(\boldsymbol{w}_h)) \, \mathrm{d}\Omega - \int_\Omega \nabla\varphi_i \cdot \boldsymbol{V}(\boldsymbol{w}_h) r \, \mathrm{d}\Omega$$
$$= \int_\Omega \Omega_c(\boldsymbol{w}_h)\varphi_i r \, \mathrm{d}\Omega - \int_{\partial\Omega} r\boldsymbol{V}(\boldsymbol{w}_h)\varphi_i \cdot \boldsymbol{n} \, \mathrm{d}\Gamma + \int_\Omega \boldsymbol{S}(\boldsymbol{w}_h)\varphi_i \, \mathrm{d}\Omega \tag{18}$$

for admissible test functions φ_i with compact support on patch C_i centered at node i. The convective flux treatment in the second integral is carried out following the approach in the next section. Further details are given in Reference [14].

3. OSHER APPROXIMATE RIEMANN SOLVER

3.1. Flux function

The convective flux term in (18) is first rewritten as a boundary integral,

$$\int_{C_i} \nabla\cdot(r\boldsymbol{F}(\boldsymbol{w}_h)) \, \mathrm{d}\Omega = \int_{\partial C_i} \boldsymbol{F}(\boldsymbol{w}_h)\cdot\boldsymbol{n} r \, \mathrm{d}l = \sum_{j\in\kappa_i} \int_{S_{ij}} \boldsymbol{F}(\boldsymbol{w}_h)\cdot\boldsymbol{n} r \, \mathrm{d}l \tag{19}$$

where κ_i is the set of element neighbors of node i, ∂S_{ij} is the bi-segment joining the midpoint of segment ij to the centroids of the triangles for which the segment ij is a side and $\boldsymbol{n}$ is the normal to the segment (Figure 1).

The flux function defined by the relation

$$F_{ij}(\boldsymbol{w}_\mathrm{L}, \boldsymbol{w}_\mathrm{R}) = \int_{S_{ij}} \boldsymbol{F}(\boldsymbol{w}_h)\cdot\boldsymbol{n} r \, \mathrm{d}l \tag{20}$$

may be computed using approximate Riemann solvers [15,16] or flux vector splitting schemes [17,18]. These techniques were originally developed to solve the Euler equations for a perfect gas, and have been extended here to non-equilibrium reacting gas problems. More specifically,

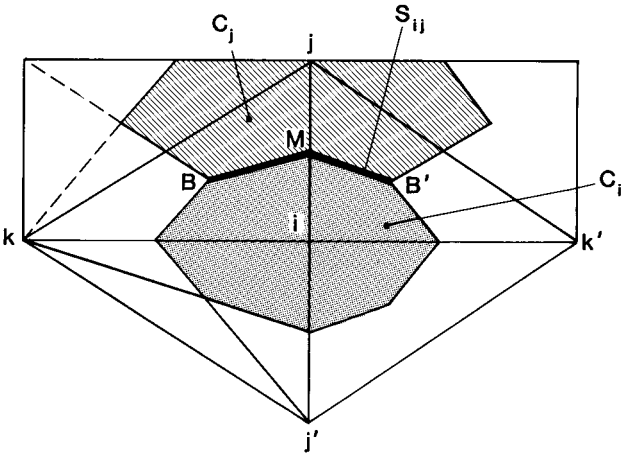

Figure 1. Dual mesh: triangulation and finite volume cell C_i.

the numerical flux function in (20) is approximated by an extension of Osher's upwind scheme, following the approach by Abgrall [13] for non-equilibrium reacting flows, and is further modified for the axisymmetric problem. We remark that this approximate Riemann solver involves more complex calculations to evaluate the dissipation terms of the flux function than the approximate Riemann solver of Roe [16]. However, it does not require an 'entropy correction' [19], and is more robust for non-linear waves.

It is difficult to derive the Osher flux function rigorously for the reacting gas problem and some simplifications are required in the evaluation of the Jacobian matrix and the Riemann invariants; e.g. the matrix is derived assuming that all components of the variable vector $\boldsymbol{w}$ are independent. This is not strictly true since, in the case of chemical equilibrium, the densities of species are coupled by the equilibrium constants of the chemical reactions. Thus, it is not possible to argue that the density of a given species is independent of the other densities, and the overall energy of the gas. Other examples of constraints on the densities occur because of atom and charge conservation. The ratio of nitrogen atoms to oxygen atoms is fixed at the value in standard air (79:21), and the plasma is assumed to be neutral.

3.2. Riemann invariants and intermediate states

General definitions of the Osher–Riemann solver invariants and intermediate states are given in Reference [15]. The Riemann invariants are determined from the eigenvalues of the Jacobian $\mathbf{A}$ of the convective flux $\boldsymbol{F}(\boldsymbol{w}_h)\cdot\int_{\partial S_{ij}} \boldsymbol{n}r \, \mathrm{d}l$, and the right eigenvectors associated with each eigenvalue. The eigenvalues of $\mathbf{A}$ are $\hat{u}$, $\hat{u}+a$ and $\hat{u}-a$, where the pseudo-velocity is defined by

$$\hat{u} = \boldsymbol{u}\cdot\int_{\partial S_{ij}} \boldsymbol{n}r \, \mathrm{d}l = \boldsymbol{u}\cdot\boldsymbol{v} \tag{21}$$

and the pseudo-speed of sound is defined by

$$a^2 = \gamma_{so}\frac{p}{\rho}, \quad \gamma_{so} = \frac{\sum_i \rho_i \dfrac{R_g}{M_i}}{\sum_i \rho_i c_{vi}} \tag{22}$$

The Riemann invariants for $\hat{u} \pm a$ are

$$\frac{\rho_i}{\rho} = \text{constant}, \qquad \frac{E_{v1}}{\rho} = \text{constant} \quad \text{and} \quad \hat{u} = \text{constant} \tag{23}$$

$$\hat{u} \mp \frac{2a}{\gamma_{so} - 1} = \text{constant} \quad \text{and} \quad \frac{p}{\rho^{\gamma_{so}}} = \text{constant} \tag{24}$$

For $\boldsymbol{u} \cdot \boldsymbol{v}$, we get the invariants

$$\hat{u} = \text{constant} \quad \text{and} \quad p = \text{constant} \tag{25}$$

The intermediate points and sonic points, when they exist, are determined using the Riemann invariants. Furthermore, the eigenvalues at the sonic points are equal to zero. In this work, we choose to order the eigenvalues as follows: $\hat{u} + a$, $\hat{u}$, $\hat{u} - a$; this order is important for the calculation of the Osher flux [15]. Expressions for the intermediate states and sonic points are given in Reference [14]. In the previous derivations of the approximate Riemann invariants, the intermediate states and sonic points, the only necessary assumption is that γ_{so} is constant through a compression or a rarefaction wave. Abgrall *et al.* [13] derived the Riemann invariants and intermediate states for one-dimensional non-equilibrium flows. They added for the $\hat{u} \pm a$ waves, another Riemann invariant equal to p/ρ^{γ_e}, where γ_e is assumed constant and defined in their work.

4. BOUNDARY CONDITIONS

At the axis of symmetry we set $\boldsymbol{u} \cdot \boldsymbol{n} = 0$. The walls may be fully catalytic or non-catalytic, at constant temperature or adiabatic. The velocity at the walls is set to zero; the normal gradient of the vibrational temperature is taken to be zero, as discussed by Park [20]. For far-field boundary conditions, where we have specified incoming profiles or exit free conditions, Fezoui and Stoufflet [12] suggested the use of a Steger and Warming splitting approximation, which implies

$$\int_{\partial C_i \cap \partial\Omega} \boldsymbol{F} \cdot \boldsymbol{n} r \, \mathrm{d}l = \mathbf{A}^+(\boldsymbol{W}_i)\boldsymbol{W}_i + \mathbf{A}^-(\boldsymbol{W}_i)\boldsymbol{W}_\infty \tag{26}$$

where $\mathbf{A}^+$ and $\mathbf{A}^-$ are defined from the Jacobian matrix $\mathbf{A}$ of

$$F_{i\infty} = \boldsymbol{F}(\boldsymbol{W}) \cdot \int_{\partial C_i \cap \partial \Omega} \boldsymbol{n} r \, \mathrm{d}l \tag{27}$$

Matrices $\mathbf{A}^+$ and $\mathbf{A}^-$ have the same eigenvectors as $\mathbf{A}$; the eigenvalues of $\mathbf{A}^+$ are the positive eigenvalues of $\mathbf{A}$, the eigenvalues of $\mathbf{A}^-$ are the negative eigenvalues of $\mathbf{A}$. Furthermore, they satisfy the equality $\mathbf{A} = \mathbf{A}^+ + \mathbf{A}^-$. The matrices $\mathbf{A}^+$ and $\mathbf{A}^-$ need not be computed explicitly because of the following identity:

$$\mathbf{A}\mathbf{w} = \lambda_1 \mathbf{w} + \sum_{i>1} (\lambda_i - \lambda_1)(\mathbf{l}_i \cdot \mathbf{w})\mathbf{r}_i \tag{28}$$

where λ_i are eigenvalues of $\mathbf{A}$, and $\mathbf{l}_i$, $\mathbf{r}_i$ are, respectively, the left and right eigenvectors associated with λ_i. $\mathbf{A}^+$ and $\mathbf{A}^-$ satisfy the same equation, replacing the eigenvalues accordingly. Hence, Equation (28) may be used to determine the matrices $\mathbf{A}^+$ and $\mathbf{A}^-$ by replacing $\mathbf{w}$ successively by the vectors of the canonical basis.

5. SOLUTION ALGORITHM

A time-dependent formulation of the problem has been developed. This implies that both unsteady and steady solutions can be computed. For the steady state problem it is not necessary to obtain an accurate time-dependent solution, and large time steps are desirable. However, since the chemical characteristic time is several orders of magnitude smaller than the acoustic relaxation time, the chemical source terms are treated using a semi-implicit approach. We approximate the unsteady term by a first-order discretization in time, and use mass lumping to rewrite the unsteady, axisymmetric and non-equilibrium source terms in Equations (19) and (20).

$$\left(\boldsymbol{I} - \Delta t \frac{\partial \Omega_c}{\partial \boldsymbol{W}}\right) \frac{\Delta \boldsymbol{W}_i}{\Delta t} r_i \int_{C_i} \mathrm{d}A = (\Omega_c(\boldsymbol{W}_i) r_i + \boldsymbol{S}(\boldsymbol{W}_i)) \int_{C_i} \mathrm{d}A - \sum_{j \in \kappa(i)} \varphi F_{ij} - \int_{\Omega} r \boldsymbol{V}(\boldsymbol{W}_h) \cdot \nabla \varphi_i \, \mathrm{d}A + \int_{\partial \Omega} r \boldsymbol{V}(\boldsymbol{W}_h) \varphi_i \cdot \boldsymbol{n} \, \mathrm{d}\Gamma \tag{29}$$

or more compactly,

$$\mathbf{M} \Delta \boldsymbol{W} = \mathbf{B} \tag{30}$$

where $\mathbf{M}$ is a block diagonal matrix, $\Delta \boldsymbol{W}$ is a vector with components $\Delta \boldsymbol{W}_i$, and the components of $\mathbf{B}$ correspond to the right-hand-side of Equation (29). The convective flux, φF_{ij}, computed in the explicit scheme by the Osher upwind scheme defined above, may also be approximated by the Steger and Warming flux function,

$$\varphi F_{ij}(\boldsymbol{U}, \boldsymbol{V}) = A_{ij}^{+}(\boldsymbol{U})\boldsymbol{U} + A_{ij}^{-}(\boldsymbol{V})\boldsymbol{V} \tag{31}$$

where A_{ij} is defined by $F_{ij}(\boldsymbol{U}) = A_{ij}(\boldsymbol{U})\boldsymbol{U}$ and $A_{ij} = A_{ij}^{+} + A_{ij}^{-}$, where the eigenvalues of A_{ij}^{+} are the positive eigenvalues of A_{ij}, and the eigenvalues of A_{ij}^{-} are the negative eigenvalues of A_{ij}. This allows us to compute an approximate Jacobian of φF_{ij},

$$\partial\varphi F_{ij}(\boldsymbol{U}, \boldsymbol{V})(\delta\boldsymbol{U}, \delta\boldsymbol{V}) = A_{ij}^{+}(\boldsymbol{U})\delta\boldsymbol{U} + A_{ij}^{-}(\boldsymbol{V})\delta\boldsymbol{V} \tag{32}$$

Now the problem reduces to solving the matrix system $\mathbf{M}'\Delta\boldsymbol{W} = \mathbf{B}$, where $\mathbf{M}' = \mathbf{M} + \mathbf{M}''$, is no longer block-diagonal. This system is solved using a block Jacobi algorithm.

Remark

Even though it is possible to derive the Jacobian matrix A_{ij} analytically, assuming that the components of the vector of conservative variables $\boldsymbol{W}$ are linearly independent, analytic expressions A_{ij}^{+} and A_{ij}^{-} are not obvious. Since the eigenvalues and eigenvectors of A_{ij} are known, we may obtain the matrices A_{ij}^{+} and A_{ij}^{-} using Equation (28). The viscous flux is linearized using an analytically derived approximate Jacobian operator. When deriving the viscous Jacobian we neglect the variations of transport properties (viscosity, thermal and vibrational conductivities).

6. HYPERSONIC FLOW PAST A TWO-DIMENSIONAL SEMI-ELLIPSE

The goal of this test problem is to compare inviscid perfect gas calculations with inviscid reacting gas calculations for a two-dimensional hypersonic flow past a profile with an elliptic nose at an angle of incidence of 30°. The reacting gas is assumed to be out of chemical equilibrium, but in thermal equilibrium. This test problem was proposed in Reference [21].

The semi-ellipse is defined by the equation $(x/0.06)^2 + (y/0.015)^2 = 1$. The mesh is generated by mapping from a structured grid (90×30) and is slightly graded near the nose of the ellipse. The incoming flow at angle of incidence is specified by the following characteristics $M_\infty = 25$, $T_\infty = 205.3$ K and $p_\infty = 2.52$ Pa. The pressure and temperature correspond to standard atmospheric conditions at an altitude 75 km. For perfect gas calculations, we assume that the mole fractions of N_2 and O_2 are in the ratio 79:21. For reacting gas calculations, we consider a five-species gas composed of N_2, O_2, NO, N and O. The corresponding set of chemical reactions is given in Appendix A of Part I. The initial data are taken as the approximate solution for flow at zero angle of incidence. Incremental continuation in incidence angle is used to finally reach the 30° incidence condition in 50 steps. This approach avoids stability problems due to negative numerical pressure values, which arise in the first steps of the calculations if the 30° incidence is enforced immediately.

We ran a validation test case on the simpler problem of a flow over a circular cylinder of radius 0.05, at Mach 10 with no angle of incidence. The same incoming flow characteristics as the one mentioned above were used. For such a case, the shock stand-off distance δ is known by the empirical formula $\delta/R = 0.386\exp(4.67/M_\infty^2) = 0.4044$, where R is the radius of the cylinder and M_∞ is the incoming Mach number. Also, the maximum stagnation temperature is determined by $T/T_\infty = 1 + (\gamma - 1)/2M_\infty^2$, so $T = 2258.3$ K, where T_∞ is the incoming flow temperature. The 50×100 mesh is structured. The maximum temperature computed is 2162 K.

Applying a first level of refinement with an error indicator based on the pressure gradient, the new maximum temperature behind the shock is 2217 K, which is within 2% of the exact value of the maximum temperature. The shock distance ratio δ/R is equal to 0.398.

Figure 2 compares the temperature profile on the symmetry line of the ellipse obtained for two meshes: a coarse grid and a refined mesh adapted from the coarse mesh with an error indicator based on the pressure gradient. We note that in this problem, due to the angle of incidence, the symmetry line is different from the stagnation line. The shock stand-off distance of 3.27 mm, obtained in this calculation with a refined mesh, shows 10% improvement on 3.6 mm obtained on the coarse structured grid. This shows clearly that the shock stand-off distance depends on the shock resolution and grid resolution.

This difference of prediction between computations on a crude grid, and on an adapted grid raises a conceptual issue: rather than seeking a uniformally small error in the flow domain, we may seek a small error in the domain of interest to, say, the designer. In this example, we are interested in the accuracy of the solution around the axis of symmetry where the temperatures are the largest, and do not need a great accuracy for the shock resolution in other regions. Smeared shocks, singularities, far-field approximations can be inaccurate provided that they do not pollute the approximation in the domain of interest [22].

A calculation was performed assuming that the gas is in thermal equilibrium. The maximum temperature behind the shock is $T = 18900$ K. The chemistry at this temperature is endoergic, because the principal reactions result in dissociation of the molecular species. Therefore, as expected, the maximum computed temperature is lower than that predicted for an inert gas.

Ionization is significant at the conditions of the test problem. Figures 3 and 4 show results for a reacting and ionizing flow past the ellipse for a five-species and a nine-species gas, respectively at thermal equilibrium. Iterations for both five-species and nine-species calculations were terminated at a residual less than 10^{-3}. The temperature contours in Figures 3 and

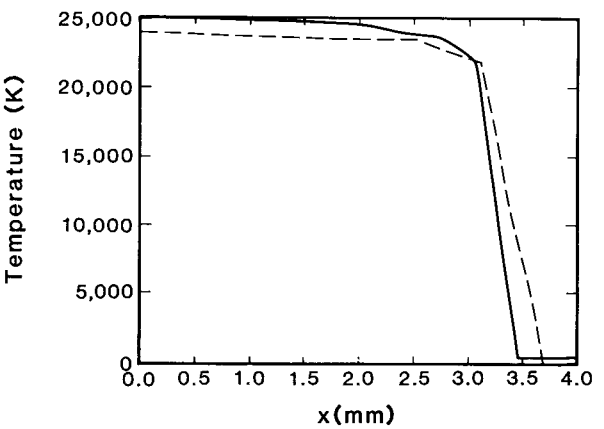

Figure 2. Translational temperature comparison for coarse and refined meshes on the symmetry line for a perfect gas $M = 25$ flow over an ellipse.

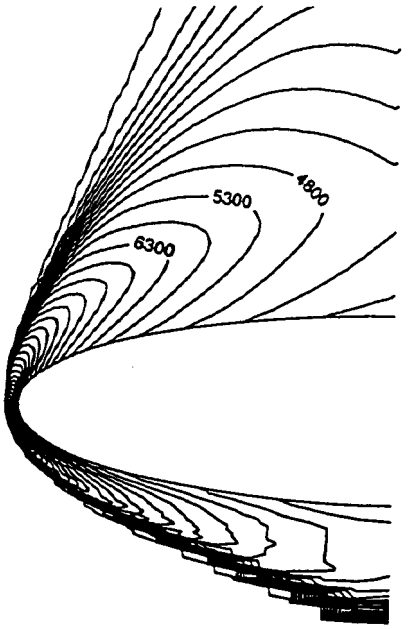

Figure 3. Isotherms for a five-species thermally equilibrated chemically reacting flow past a two-dimensional semi-ellipse.

4 show that at a given location behind the shock, the translational temperature for the nine-species model is less than that for the five-species model. This difference may be explained by the fact that highly endoergic ionization reactions are included in the nine-species model, which tend to lower the gas temperature.

7. HYPERVELOCITY FLOW PAST A HEMISPHERICALLY TIPPED BODY AT SEA LEVEL

This series of problems presents results and analyses of non-equilibrium calculations of a reacting air flow around a hemispherically tipped body with nose radius $R = 1-100$ mm. The velocity v_∞ of the incoming flow varies from 2 to 10 km s^{-1}. The conditions for pressure and temperature are those at an altitude z.

The purpose of this analysis is to determine a domain in the three-dimensional space (R, v_∞, z) for which the flow field in the shock layer may be defined by two properties.

We note that this domain has equivalent domains when we replace any of the radius, velocity or altitude by the Reynolds number based on the radius R: $Re = v_\infty R/v(z)$.

We consider two cases for which the knowledge of two physical properties is sufficient to characterize the gas locally. The first occurs when the gas is locally in thermal and chemical

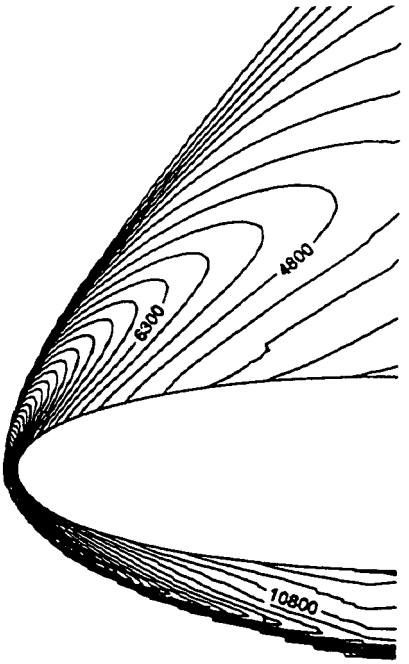

Figure 4. Isotherms for a nine-species reacting air calculation.

equilibrium; then the composition of the flow is obtained knowing the equilibrium constants of the chemical reactions. In a second case, the gas is frozen at the composition of ambient air for temperatures less than 1000 K: the mass fractions of species NO, N and O are negligible compared with the mass fractions of N_2 and O_2. The knowledge of pressure and enthalpy, for instance, is then sufficient to obtain any other local properties of the gas.

These domains will guide design engineers who need to study the high speed flow patterns around a blunt nosed body. For a specified radius, velocity and altitude, we can determine what type of model and simulator will suffice to provide a satisfactory computation of the flow field, depending on which part of the domain this set belongs to.

Such considerations are important for design purposes, since for a suitable problem, a perfect gas code will provide a solution much faster than a full non-equilibrium flow code.

7.1. Calculations at sea level

Here we consider non-equilibrium viscous flow past a sphere at sea level. For this test case, the non-equilibrium source term is important since the density at sea level is high: $1.14\,\mathrm{kg\,m^{-3}}$ compared with $4.674 \times 10^{-5}\,\mathrm{kg\,m^{-3}}$ at an altitude of 75 km. The problem is two-dimensional axisymmetric. The sphere has a radius of 1 mm. The solution presented in this paper is computed on a crude mesh (1701 nodes), graded towards the stagnation point. The first node

on the stagnation line is at a distance 10^{-6} m from the sphere. The characteristics of the incoming flow are $v_\infty = 2\ \mathrm{km\ s^{-1}}$, $p_\infty = 1$ atm, $T_\infty = 298$ K. The wall is adiabatic and non-catalytic, the incoming air flow is considered inert, and the vibrational temperature of the gas is taken as $T_v = 298$ K. Since the maximum temperature behind a normal shock, at $M_\infty = 5.68$, is 2150 K for a perfect gas, only a five-species gas calculation is performed: the ionization reactions are negligible at temperatures less than 2500 K in air. The composition of the free-stream flow is the equilibrium composition at $T = 1000$ K, since the composition of the chemical reactions is forced to be constant at temperatures lower than 1000 K.

Figure 5 shows the translational temperature contours. Figure 6 shows a clear difference between the translational and vibrational temperatures along the stagnation line, which indicates that the flow is out of thermal and chemical equilibrium. This observation was confirmed with several calculations on more refined grids. At the conditions of the flow behind the shock ($T_{\max} = 2200$ K, $p_{\max} = 42$ kPa), the vibrational relaxation time $\tau_{v,N_2N_2} = O(10^{-5})$ s, whereas the flow characteristic time at the middle of the shock layer τ_{flow} is of the order of 10^{-6} s. This explains why the flow is out of thermal equilibrium in the shock layer at the conditions of this test case.

The density contours of NO around the hemispherically blunt body are given in Figure 7 for inviscid calculations. The density increases as the temperature increases behind the shock. The flow is out of chemical equilibrium: at $T = 2000$ K, the equilibrium density of NO is approximately 10^{-3}, whereas in the current calculations, the density of NO reaches a

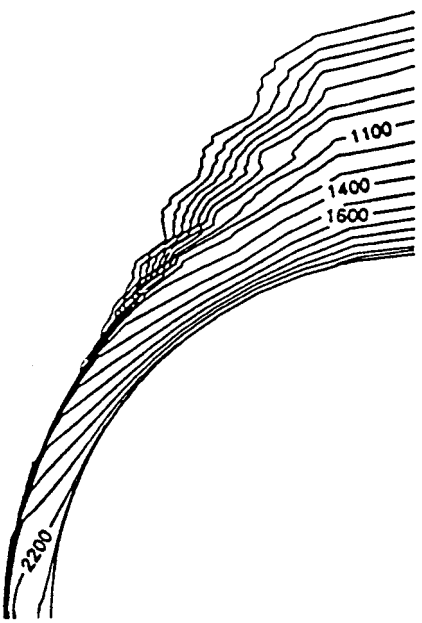

Figure 5. Translation temperature isolines.

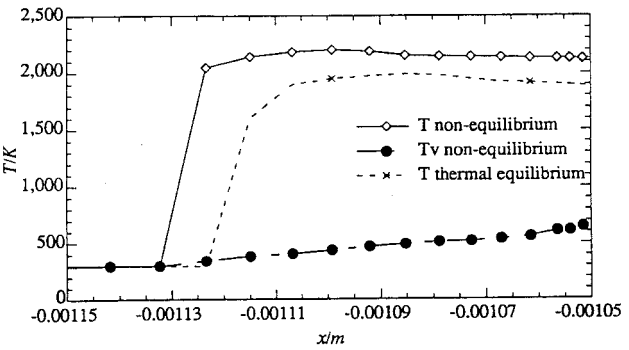

Figure 6. Stagnation line temperature comparison.

maximum value of the order of 10^{-6}. This is due to the fact that the set of chemical reactions $N + O_2 \rightarrow NO + O$ and $N + NO \rightarrow O + N_2$ are predominant and are not equilibrated. NO is depleted to produce O atoms and N_2.

7.1.1. Influence of the physical model. Figure 6 also compares the temperature along the stagnation line for two inviscid flow calculations: (i) full non-equilibrium, and (ii) thermal equilibrium ($T_v = T$) but chemical non-equilibrium. In case (ii), the rate coefficients depend

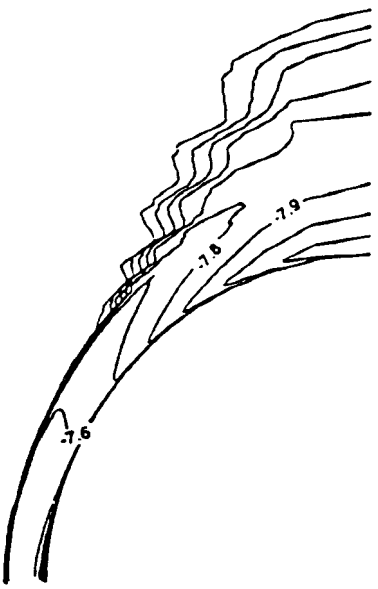

Figure 7. Log_{10}(NO) density contours.

only on the translational temperature. Both calculations are converged to a residual of 10^{-3}. These calculations required more than 3000 iterations at a Courant–Friedrich–Lewy (CFL) number of 0.1. The non-equilibrium calculation is performed using the thermal equilibrium calculation as a 'warm start'. The maximum temperature for the non-equilibrium calculation is 2200 K versus 2000 K for the thermal equilibrium calculation. The translational temperature is lower in the case of thermal equilibrium since the vibrational energy is higher than that for a non-equilibrium calculation.

It is emphasized that the vibrational–translational (V–T) relaxation time model used in these calculations follows the Millikan and White curve-fit formulae. The model of Thivet *et al.* [23] significantly modifies the vibrational temperature since it gives a shorter V–T relaxation time than the Millikan and White model. This will affect the nature of the flow in the shock layer since a shorter relaxation time will lead to thermal equilibrium faster. However, in the absence of experimental data, it is not clear which model is preferable.

7.1.2. Influence of the grid. The effect of the grid on two main features of the flow was investigated in this calculation. First, the nature of the flow in the shock layer was examined. It was observed that the shock stand-off distance was insensitive to the grid as well as to the nature of the flow in the shock layer. Second, to obtain accurate gradients at the wall and near the stagnation line, calculations required a very fine grid. Several parameters were studied, including the effect of cell aspect ratios at the wall, the distance of the first node away from the wall, and the number of nodes in a boundary layer. We observed that the choice of a first cell at the stagnation line with a ratio $\delta y/R = O(10^{-5})$, where R is the radius of the body at the nose, gave gradients independent of the cell width in the radial direction, δy. Owing to the first-order accuracy of the numerical scheme, the aspect ratio of the cell was kept less than $\delta y/\delta r = 5$. The explicit scheme failed to converge for a CFL number larger than 0.1 when the aspect ratio exceeded 20. The first ten points away from the wall were positioned to be equidistant along the stagnation line.

7.1.3. Parametric study. In this section, we present results of calculations for varying radii, $R = 1$–100 mm, at incoming flow velocities $v_\infty = 2$–10 km s^{-1}. The wall conditions are similar to those discussed in the particular test case presented above. The physical model chosen corresponds to the model used in the previous calculation. In order to perform viscous calculations predicting wall gradients, the mesh is structured with 100×60 nodes.

The shock distance as a function of incoming velocity, computed using the formulae of Reference [24] is compared in Figure 8 with the present solution. Differences of up to 30% are observed. This discrepancy is largely due to the fact that Reference [24] assumes a calorifically perfect gas (which is clearly not the case here). It is also observed that the results obtained fit the relation

$$\frac{\delta}{R} = \frac{2}{3}\frac{\rho_b}{\rho_\infty} \tag{33}$$

with δ the stand-off distance, R the radius at the nose, and ρ_b the density behind the shock.

As a reference, note that the work of Wen and Hornung [25] presents a correlation between the shock stand-off distance around a sphere with the free-stream kinetic energy and a reaction

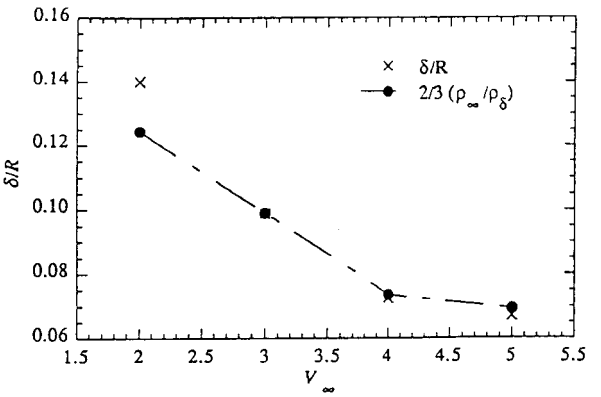

Figure 8. Shock stand-off distance × for $R = 1$ mm, at sea level conditions compared with Reference [24].

rate parameter. This work was validated and studied for incoming flow pressures and temperatures, different by orders of magnitude from the pressure and temperature conditions of the current study.

For each calculation performed, a sub-layer was observed in the shock layer in which the translational and vibrational temperatures are equal. This remark validates simplifying assumptions of the flow physics in the shock layer, used for instance in the work of Wen and Hornung [25] to derive analytical closed form relations. This layer is termed the thermal equilibrium layer.

Figure 9 shows the ratio of the thermal equilibrium layer thickness to the shock stand-off distance, ζ/δ, along the stagnation line for a radius $R = 1$ mm, as a function of incoming flow velocity or the Reynolds number.

It is noted that for large velocities ($\geq 5\ \mathrm{km\ s^{-1}}$), the shock layer is nearly completely in thermal equilibrium, whereas for lower velocities, a significant portion of the layer is out of thermal equilibrium. However, it is also noted that for velocities less than $2.5\ \mathrm{km\ s^{-1}}$, the flow behind the shock is frozen at a composition equal to the ambient air composition. Hence, for a five-species gas model for air (N_2, O_2, NO, N, O), the mass fractions of NO, N, O are much less than 10^{-4}. Since at such velocities, the equilibrium mass fractions of NO, N and O are negligible, we can still characterize the flow field composition with only two properties (e.g. pressure and enthalpy).

Several calculations were performed at sea level, and are reported in Figure 10. When the maximum temperature behind the shock is larger than 6000 K, a nine-species model for air including ionization is needed. When the maximum temperature is less than 6000 K, a five-species air model suffices. From these calculations it is possible to define a zone in the (R, v_∞) plane for which the shock layer is fully in chemical and thermal equilibrium. Also, for velocities less than $2.5\ \mathrm{km\ s^{-1}}$ at sea level (which corresponds to a maximum temperature $T = 2500$ K behind the shock), for the conditions at sea level the flow is considered frozen, as

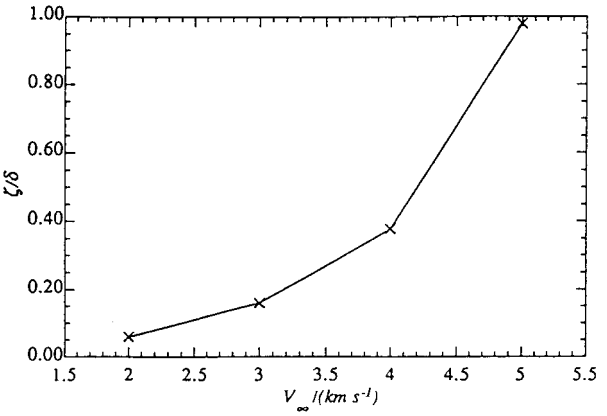

Figure 9. Thermal equilibrium layer distance over shock stand-off distance for $R = 1$ mm, at sea level conditions.

described above. The limit of this frozen shock layer zone is not absolute since it is clear from the previous remarks that the calculations are dependent on the physical model.

In Figure 10, the line $v_\infty = 2.5\ \mathrm{km\ s^{-1}}$ intersects the boundary separating equilibrium and non-equilibrium shock layers. At temperatures less than 2500 K, the equilibrium concentrations of NO, N and O are negligible in front of the concentration of N_2 and O_2. The approximation of frozen flow also considers that the concentrations of NO, N and O are negligible. It is, therefore, possible to assume a frozen shock layer, even though this is not strictly true theoretically.

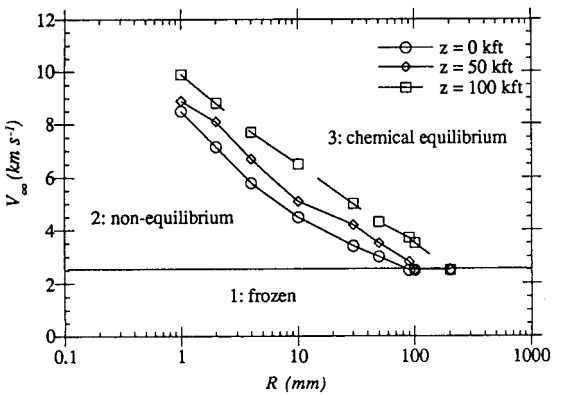

Figure 10. Mapping of equilibrium, non-equilibrium and chemically frozen regions as a function of altitude, incoming flow velocity and nose radius.

Table I. Velocity gradient comparison.

v_∞ (km s^{-1})	$(du/ds)_{s=0}$ (s^{-1})	$(\rho_\infty/\rho_{\text{shock}})^{1/3} = \epsilon^{1/3}$	$\epsilon^{1/3}/[(R/v_\infty)(du/ds)_{s=0}]$
2.0	1.09×10^{-6}	5.77×10^{-1}	1.059
3.0	1.39×10^{-6}	5.43×10^{-1}	1.172
4.0	1.71×10^{-6}	4.87×10^{-1}	1.14
5.0	2.05×10^{-6}	4.73×10^{-1}	1.15

For a small radius, the shock layer is in thermal equilibrium at high velocities, whereas for large radii, the shock layer is in thermal equilibrium for all velocities.

Note that no experimental data is available to validate the flow field properties and wall gradients. However, Reinecke [26] fitted experimental results and calculations performed over the past 30 years to obtain a formula for the velocity gradient at the stagnation point,

$$\left(\frac{\rho_\infty}{\rho_{\text{shock}}}\right)^{1/3} = \frac{R}{v_\infty}\left(\frac{\mathrm{d}u}{\mathrm{d}s}\right)_{s=0} \tag{34}$$

where s is the curvilinear co-ordinate along the sphere, R is the radius at the nose, and ∞ denotes incoming flow properties. The results obtained from these calculations are presented in Table I. The calculations show agreement within 6–17 per cent.

7.2. Mapping as a function of altitude

The flow field around a hemispherically tipped body of radius R depends on the incoming flow velocity, pressure and temperature for a perfect gas. For the range of incoming flow velocities ($v_\infty \in [2, 10$ km s$^{-1}]$) of interest in this test problem, the predominant chemical reactions behind the shock are binary dissociation reactions; binary scaling may be used to characterize the flow in the shock layer when the whole shock layer is in thermal equilibrium. Binary scaling does not apply, however, for thermal non-equilibrium problems. More computations are therefore necessary to establish a mapping in the (R, v_∞, z) domain, showing regions in which the shock layer properties may be characterized by only two physical properties. A series of computations with incoming flow conditions corresponding to altitudes of $z = 50$ kft and $z = 100$ kft were performed; Table II gives the properties at the altitudes considered here.

The domains are presented in Figure 10. All three altitudes are overlapped on this figure, showing the overlapped domains in the (R, v_∞) plane. Three zones are distinguished. In the

Table II. Incoming flow properties.

z (kft)	p (atm)	ρ (kg m^{-3})	T (K)
0.0	1.0	1.14	298.0
50.0	0.1156	0.1822	216.0
100.0	0.0118	0.0173	232.0

zone denoted 1, the flow in the shock layer is chemically frozen, so a perfect gas code will be sufficient to compute the flow properties.

The velocity threshold at which the maximum translational temperature behind the shock reaches 2500 K increases weakly with altitude. It is shown as constant for the sake of clarity on the figure. It is observed that at $z = 0$ kft, the temperature behind the shock reaches 2500 K for an incoming velocity of 2390 m s^{-1}, while at $z = 50$ kft and $z = 100$ kft, the velocity threshold is 2430 and 2470 m s^{-1} respectively. Changes in the physical model, or the use of an adaptive mesh, may modify these numbers since the peak temperature behind the shock is sensitive to the reaction rate coefficients, as well as the shock resolution.

The zone denoted 3 is defined above the curves dependent on the altitude. In this zone, the shock layer is in chemical equilibrium. Between the chemical equilibrium case and the frozen flow case is zone 2, for which the shock layer is neither frozen nor in chemical equilibrium. A full non-equilibrium numerical code is needed to compute the properties of the flow in this zone.

The mapping as a function of altitude also indicates that the zone of non-equilibrium in the (R, v_∞) plane increases with altitude. At a fixed radius and incoming velocity for a given temperature behind the shock, the V–T relaxation time is inversely proportional to the pressure, and hence increases with altitude. Thermal non-equilibrium is then stronger as the altitude increases.

8. CONCLUDING REMARKS

In this part, a hybrid finite element/finite volume–$P1$ formulation is developed and implemented to solve the two-dimensional axisymmetric Navier–Stokes equations for a multi-species reacting gas out of thermal and chemical equilibrium. This work is an extension of the approaches in References [12,27]. The scheme employs a semi-implicit treatment of the convective and viscous fluxes to permit larger time steps when marching to the steady state solution. However, in the solutions of the $M = 25$ flow over a two-dimensional ellipse and flow in the test section of a plasma torch, a CFL number of less than 20 had to be employed to obtain a converged solution. Most of the calculations were performed using the first-order approximate solver. However, this code is less reliable for boundary layer calculations with high triangle aspect ratio. For these test problems a discrepancy of 10–15 per cent was observed between the numerical results from this work and experimental or theoretical data, with triangle aspect ratios greater than 500. Implementation of a second-order-accurate scheme gives better results for perfect gas calculations [14]. Future work is needed to develop an improved second-order scheme for non-equilibrium calculations. The Osher approximate Riemann solver employed to treat the convective flux is computationally more expensive than a Roe approximate solver. However, it does allow computation of highly non-linear flows, such as the $M = 25$ strong shock problem for the two-dimensional ellipse even on a relatively coarse mesh. An adaptive refinement procedure would give better resolution of shocks and flow details.

ACKNOWLEDGMENTS

The authors would like to thank Dr Harry Fair, Dr Hans Mark and Dr Bill Reinecke at IAT for their support and suggestions in this work. This work was supported under ARDEC/ARL contract DAAA21-93-C-0101, ARPA Grant # DABT63-92-C-0024, Advanced Technology Program, # 089, and ASCI grant # B347883.

REFERENCES

1. Desideri JA, Glowinski R, Periaux J (eds). *Hypersonic Flows for Reentry Problems*, vols. I and II. Springer: Berlin, 1991.
2. Hunt JJ (ed). *Second European Symposium on Aerothermodynamics for Space Vehicles*, November 1994. ESA SP-367, Noordwijk, The Netherlands, 1995.
3. Dervieux A, Larrouturou B (eds). *Numerical Combustion: Proceedings of the Third International Conference on Numerical Combustion*. Springer: Berlin, 1989.
4. Gnoffo PA. *A code calibration program in support of the Aeroassist Flight Experiment*. AIAA Paper 89-1799, 1989.
5. Chiang TL. *Computation of nonequilibrium chemically reacting flows in hypersonic flow field*. PhD Thesis, Aerospace Engineering, The University of Texas at Austin, 1989.
6. Candler G. *The computation of weakly ionized hypersonic flows in thermochemical nonequilibrium*. PhD Thesis, Stanford University, 1988.
7. Rostand P, McCormack RW. *CFD modeling of an arc heated jet*. AIAA 21st Fluid Dynamics, Plasma Dynamics, and Lasers Conference, AIAA Paper 90-1475, Seattle, WA, June 1990.
8. Suresh A, Liou M. *The Osher scheme for real gases*. 28th Aerospace Sciences Meeting, AIAA Paper 90-0397, January 1990.
9. Grossman B, Cinnella P. Flux split algorithms for flows with non-equilibrium chemistry and vibrational relaxation. *Journal of Computational Physics* 1990; **88**: 131–168.
10. Chalot F, Hughes TJR, Johan Z, Shakib F. Application of the Galerkin/least squares formulation to the analysis of hypersonic flows. In *Hypersonic Flows for Reentry Problems*, vol. II, Desideri JA, Glowinski R, Periaux J (eds). Springer: Berlin, 1991; 427–450.
11. Angrand F, Dervieux A. Some explicit triangular finite element schemes for the Euler equations. *International Journal for Numerical Methods in Fluids* 1984; **4**: 749–764.
12. Fezoui L, Stoufflet B. A class of implicit upwind schemes for Euler simulations with unstructured meshes. *Journal of Computational Physics* 1989; **84**: 174–206.
13. Abgrall R, Fezoui L, Talandier J. An extension of Osher's Riemann solver for chemical and vibrational non-equilibrium gas flows for the Euler equations. *International Journal for Numerical Methods in Fluids* 1992; **14**: 935–960.
14. Harle C. *Navier–Stokes computations for non-equilibrium reacting gas flows*. PhD Thesis, Department of Aerospace Engineering, The University of Texas at Austin, August 1994.
15. Chakravarthy S, Osher S. Numerical experiments with the Osher upwind scheme for the Euler equations. *AIAA Journal* 1983; **21**: 1241–1248.
16. Roe PL. Approximate Riemann solvers, parameter vectors and difference schemes. *Journal of Computational Physics* 1981; **43**: 357–372.
17. Steger JL. *Flux vector splitting of the inviscid gas–dynamic equations with application to finite difference methods*. Technical Report NASA TM 78605, 1978.
18. van Leer B. Flux-vector splitting for the Euler equations. *Lecture Notes in Physics* 1982; **170**: 507–512.
19. Harten A. High resolution schemes for hyperbolic conservations laws. *Journal of Computational Physics* 1983; **49**: 357–397.
20. Park C. *Non-equilibrium Hypersonic Aerothermodynamics*. Wiley: New York, 1988.
21. Desideri JA, Glowinski R, Periaux J (eds). *Hypersonic Flows for Reentry Problems*, vol. I. Springer: Berlin, 1991; 225–226.
22. Carey GF. *Computational Grids*. Taylor and Francis: London, 1997.
23. Thivet F, Perrin MY, Candel S. A unified non-equilibrium model for hypersonic flows. *Physics of Fluids A* 1991; **3**: 2799–2812.
24. Anderson JD Jr. *Hypersonic and High Temperature Gas Dynamics*. McGraw-Hill: New York, 1989.
25. Wen CY, Hornung HG. Non-equilibrium dissociating flows over spheres. *Journal of Fluid Mechanics* 1995; **299**: 389–405.
26. Reinecke WG. *On the stagnation point velocity gradient on supersonic blunt bodies*. IAT.TN 0048, 1994.
27. Abgrall R, Merlo A. Calculation of a hypersonic nozzle flow. Workshop on *Hypersonic Flows for Reentry Problems*, Part II, April 1991, Antibes (France), vol 6, pp. 125–142, INRIA/GAMNI-SMAI.

